

Chemical evolution of an isolated power plant plume during the TexAQS 2000 study[☆]

Stephen R. Springston^{*}, Lawrence I. Kleinman, Frederick Brechtel¹,
Yin-Nan Lee, Linda J. Nunnermacker, Jian Wang

Brookhaven National Laboratory, Upton, NY 11973, USA

Received 2 November 2004; received in revised form 20 January 2005; accepted 20 January 2005

Abstract

Stack emissions from a coal-burning power plant were measured during a research flight of the DOE G-1 during the Texas Air Quality Study (TexAQS 2000) on 10 September 2000. Clean upstream air and an isolated location allowed the plume to be unambiguously sampled during 12 successive downwind transects to a distance of 63 km—corresponding to a processing time of 4.6 h. The chemical transformation rates of sulfur and nitrogen primary pollutants into aerosol SO_4^{2-} and HNO_3 yield independent values of OH concentration (8.0 and $11 \times 10^6 \text{ cm}^{-3}$, respectively) that are consistent within experimental uncertainty and qualitatively agree with constrained steady-state (CSS) box model calculations. Ozone production efficiency increases with plume age as expected. Primary aerosol emissions with $D_p > 5 \mu\text{m}$ were sampled near the stack. As the plume ages, aerosol size distributions adjusted for dilution show constant number concentrations of aerosols $D_p > 10 \text{ nm}$ and a marked increase in accumulation-mode particles ($D_p > 0.1 \mu\text{m}$) as gas-to-particle-conversion causes smaller particles to grow.

© 2005 Elsevier Ltd. All rights reserved.

Keywords: Power-plant plume; Texas 2000 Air Quality Study; Aerosol growth; Airborne measurements

1. Introduction

Power plants are responsible for 72 and 25% of the SO_2 and NO_x emissions in the US (EPA, 2004). Over much of the US, SO_4^{2-} constitutes 50% or more of $\text{PM}_{2.5}$, making

power plants the single largest contributor to the fine particle aerosol loading (Malm et al., 2004). A single power plant can emit more NO_x than a mid-sized city leading to high O_3 concentrations downwind. There have been many studies in power plant plumes yielding data on the formation rate of aerosol SO_4^{2-} , the oxidation rate of NO_x , and the efficiency of O_3 production, defined as the number of molecules of O_3 formed per NO_x molecule oxidized (Gillani et al., 1998; Nunnermacker et al., 2000; Hewitt, 2001; Ryerson et al., 2001). Other studies have focused on the size distributions of aerosols formed in plumes (McMurry et al., 1981; Brock et al., 2002). In only a few cases have aerosol particle size distributions, gas–gas and gas–particle conversion rates and O_3 production efficiency (OPE) been simultaneously determined.

[☆]By acceptance of this article, the publisher and/or recipient acknowledges the US Government's right to retain a non-exclusive, royalty-free copyright covering this paper. This research was performed under the auspices of the United States Department of Energy under Contract No. DE-AC02-98CH10886.

^{*}Corresponding author.

¹Now at Brechtel Mfg. Inc., 1789 Addison Way, Hayward, CA 94544, USA.

Most daytime power plant kinetic studies in cloud-free conditions show that aerosol SO_4^{2-} is formed from the oxidation of SO_2 by OH radical. Daytime NO_x oxidation is also consistent with OH chemistry, but the two measures often give different OH concentration estimates. Ozone production efficiencies have been measured in plumes with low and high NO_x emissions and under conditions where background air has low and high VOC reactivity. OPE is observed to decrease with increasing NO_x emissions and is higher in regions with biogenic isoprene emissions (Lunia et al., 2000; Ryerson et al., 2001). Evolution of aerosol size distributions in power plant plumes under cloud-free conditions is generally consistent with the accumulation of aerosol mass by a condensation process.

We report here aircraft measurements made in the Sandow power plant plume conducted as part of the TexAQS 2000 field campaign. This plant, located in rural Milam County, Texas 180 km NW of Houston, generates a total of 900 MW from four boilers burning 5.6 Mton yr^{-1} of locally produced lignite to supply electricity for a collocated aluminum smelter and the commercial power grid. The site's tallest stack is 161 m high. Stated emissions from the plant are given in Table 1. The terrain rises gradually from 141 m at the site to 160 m near the north western end of the flight track. (Elevations and aircraft altitudes are given as above mean sea level.) Vegetation was comprised of grasses and scattered trees. No significant highways or population centers impact the sampled region or the area immediately upwind.

There are several features of the Sandow plant that make it an interesting candidate to study. Sandow is remotely located, so its stack plume can be unambiguously identified and studied without interferences from other emission sources. Sandow is the largest lignite fueled power plant in the US. Compared to other fuels, lignite has a low energy content and produces fly ash that is hard to capture with an electrostatic precipitator. Combustion characteristics of lignite are different from that of other fuels as evidenced by Sandow's high CO emission rate, 21 kton yr^{-1} . SO_2 emissions are high (80 kton yr^{-1}) as 3 of the 4 units at Sandow were built in the early 1950s and were not required to meet the new

standards put into place in the 1970s. The 3 grandfathered units at Sandow are not equipped with flue gas desulfurization scrubbers and are only required to meet more lenient standards based on the sulfur content of the locally available lignite. However, these standards are slated to change.

Using data from the DOE G-1 aircraft, the conversion rate of SO_2 to aerosol sulfate was estimated by measuring an increase in aerosol volume with processing time. Changes in the NO_x to NO_y ratio were similarly used to determine the rate of NO_x oxidation. Correlations between O_x ($\text{O}_3 + \text{NO}_2$) and NO_x oxidation products ($\text{NO}_z = \text{NO}_y - \text{NO}_x$) on downwind transects of the plume were used to determine OPE. Data from optical particle probes were used to study the time evolution of the aerosol size spectra. Box model calculations are used to show how OH and OPE vary as the plume evolves from a high NO_x to a low NO_x state.

2. Experimental

On Sunday, 10 September 2000, the G-1 sampled in the plume of the Sandow power plant during 12 successive downwind transects across the power plant plume over a 1-h period corresponding to <1–63 km downwind from the stack. Within several km of the stacks, the pilots were able to navigate by reference to visual plume boundaries. Navigation further downwind was done on the basis of real-time concentration measurements. The aircraft flew at a constant speed of 100 m s^{-1} as it repeatedly crossed the plume from 14:30 to 15:40 CST. A constant pressure altitude was maintained corresponding to 590 m (roughly 450 m above the terrain). After the last perpendicular pass through the plume, the plane turned directly toward the plant and returned over the stack while climbing steadily to above the boundary layer top in order to characterize the mixing height.

3. Instruments and methods

Winds aloft were calculated from the true air speed, measured with the G-1 gust probe, and the aircraft azimuth and ground track, measured with a TANS-Vector GPS receiver (Model 3000, Trimble Navigation Limited, Sunnyvale, CA). The resulting wind velocity scalars are estimated to have a standard deviation $<0.5 \text{ m s}^{-1}$ for a 1-s time resolution.

The concentration of SO_2 was measured using a pulsed fluorescence detector (Model 43S, Thermo Electron Corporation, Franklin, MA) with enhanced flow and modified electronics to increase the response speed (Nunnermacker et al., 1998). Ambient air was

Table 1
Emissions and NO_x/SO_2 ratio

Emission inventory (kton yr^{-1})		Molar ratio (NO_x/SO_2)	
SO_2	NO_x	Inventory	Observed
80,100	25,158	0.44	0.40 (0.05) ¹

¹Average over traverses 4–12, with SO_2 and NO_y corrected for deposition losses. (Standard deviation in parenthesis).

sampled by a forward-facing inlet situated in unperturbed air 20 cm from the fuselage. A continuous, 2-m length of 1-cm i.d., PFA tubing protruded slightly from the inlet and delivered air to the instrument inlet followed by an open-split into the unpressurized cabin. System sensitivity was checked every 2 h by standard addition in ambient air yielding a 30-ppbv signal on top of the ambient signal. The RMS noise was <0.2 ppbv. The instrument was zeroed every 2 h through a K_2CO_3 impregnated filter. At typical plume concentrations we estimate a $1 - \sigma$ uncertainty of 10%. Time response is ~ 7 s.

Ozone was measured using a modified commercial UV absorption detector (Model 49-100, Thermo Electron Corporation, Franklin, MA). The inlet manifold was identical to that described for SO_2 . System sensitivity was checked every 1 h in flight against an internal O_3 source which was standardized against a NIST-traceable NO standard by gas-phase titration at the beginning and end of the program. The instrument was zeroed every hour through an internal charcoal cartridge. The RMS noise for background air was <1 ppbv.

NO , NO_2 and total NO_y were measured using a 3-channel instrument designed and constructed at BNL. The instrument measures NO directly by detecting the chemiluminescence resulting from reaction with added O_3 . NO_2 is first converted to NO by photolytic reduction followed by detection as NO . NO and NO_2 were delivered to the instrument via a PFA inlet as described above. Both sample streams passed through a 47-mm diameter, 1- μ m pore size Teflon filter at 1 SLPM. NO_y is quantified by reduction to NO in a Mo converter heated to 350 °C. The converter consists of ~ 10 g of Mo mesh in a 1.3-cm i.d. \times 15-cm length quartz tube. The tube and heater are contained in an airfoil-contoured pylon and the inlet protrudes slightly from the flat outboard end of the pylon. A ~ 1 -mm pinhole on the rounded tip of the inlet is situated in the free air stream. Calibration standards of NO and NO_2 are added to the ambient sample just inside the pinhole inlet. Total distance from the free air stream to the heated Mo mesh is <1 cm. The system sensitivity and background were regularly measured in flight for all three channels. Sensitivity was checked by standard addition of NO . Converter efficiencies for both the photolysis cell ($x = 0.348, \sigma = 0.005$), and the Mo converter ($x = 0.996, \sigma = 0.003$) were assessed by partially titrating a fraction of the NO standard with O_3 . The zero background was measured every 10 min by prereacting the ambient air with reagent O_3 . Laboratory tests demonstrate a conversion efficiency for HNO_3 of 90–95% in dry air and a 95% response time of 7 s to an instantaneous change in HNO_3 .

A TSI 3010 condensation particle counter (Thermal Systems Inc., Shoreview, MN) was used to determine the number concentration of aerosol particles with

$D_p > 10$ nm. Size distributions of accumulation-mode particles were measured by optical light scattering in 15 size bins ranging from $D_p = 0.1$ – 3μ m (PCASP-100X, Particle Measuring System, Inc., Boulder, CO). Coarse-mode particles were measured by optical light scattering in 15 size bins ranging from $D_p = 0.5$ – 8μ m (FSSP-100, Particle Measuring System, Inc., Boulder, CO). Both probes were operated in flight with the de-icing heater on at all times. Probes were calibrated against polystyrene microspheres by the manufacturer prior to the field campaign. Size bins of the PCASP were corrected for the difference in refractive index between polystyrene ($m = 1.59$) and ambient aerosol, which was assumed to be dry $(NH_4)_2SO_4$ ($m = 1.52$), using the response curves of Liu and Daum (2000). PCASP volume determined using the corrected size bins is about 20% greater than the uncorrected value. The uncertainty in aerosol number concentration and volume over the PCASP size range is qualitatively estimated as 20 and 50%, respectively, based on aircraft intercomparison flights using similar instrumentation (Moore II et al., 2004). The determination of aerosol volume from the FSSP is problematic because Mie resonances (particularly in the range $D_p = 1$ – 4μ m) do not allow the unique association between a scattering signal and a particular size particle (Leitch and Isaac, 1991; Jaenicke and Hanusch, 1993). Because of low concentrations of coarse mode particles a several minute averaging time was required to assemble reasonable statistics. Concentrations of the major inorganic ionic constituents of accumulation mode aerosols were determined from a PILS-IC (particle into liquid sampler-ion chromatography) with 3 min time resolution (Lee et al., 2003).

All real-time data were recorded on a single data system (M200, Science Engineering Associates, Willington, CT) at 1 Hz. We use the 1-s data for all subsequent analyses. To compare data between different analyzers, the raw data were adjusted in time to compensate for lags due to inlet residence, instrument mixing volumes, and electronic signal averaging. A constant time offset was determined for each system by comparing the signal to the 1-s data from the PCASP probe during transects of narrow features in an urban environment. While this procedure does not compensate for the smoothing of rapidly changing signals by slow instruments, it allows more direct comparison of fast signals (such as NO : $\tau = 2$ s and particles: $\tau < 1$ s) with slower signals (such as SO_2 : $\tau = 7$ s and O_3 : $\tau = 9$ s).

4. Results and observations

4.1. Meteorology

Widespread precipitation and relatively cool air moved through the region on 9 September the day

before this flight. Air flow was southeasterly over the Houston area bringing clouds and moisture in from the Gulf of Mexico. Weather on the flight day was mostly clear with scattered cumulus. During the transects, at a constant altitude of 590 m, the static temperature increased from 27.7 to 29.5 °C. The water vapor mixing ratio varied between 13 and 14 g kg⁻¹ corresponding to a relative humidity of 50%. The boundary layer top at 15:50 was at an altitude of 1820 m as indicated by a temperature inversion measured during the climb out of the plume at the end of sampling. Scattered cumulus clouds were widely distributed at or just above the boundary layer. Except for this, the entire mission was flown in cloud-free air.

The vector-averaged wind over the straight and level flight portions of all plume transects was 3.8 ($\sigma_{1s} = 1.2$) m s⁻¹ at 142 ($\sigma_{1s} = 24$)°. We observed no systematic changes in the wind speed or direction measured aloft at 590 m during plume sampling. Surface winds at Continuous Air Monitoring Station #601 (EPA site number: 48-149-0001) operated by Air Quality Solutions for the Lower Colorado River Authority in neighboring Fayette County were steady at 2.3 m s⁻¹ at 170° during the flight period, changing from a slightly more southerly direction in the 3 h preceding the flight. Plume age as a function of location was determined as the straight-line distance from the stack divided by the mean wind velocity. The rural area beneath the plume, both immediately upwind and downwind, was relatively free of point sources and major transportation arteries as determined by emissions maps and observations. Background levels of primary pollutants immediately upwind of the source and outside the plume edges were low, e.g.; O₃ = 55–60 ppbv, NO_x = 0.6 ppbv, and SO₂ = 0.3 ppbv.

4.2. Chemical measurements

Of the trace gases observed from the G-1, SO₂ is closest to being a zero-background conservative tracer and is therefore used to produce a picture of the spatial extent of the plume. An SO₂ time series is shown in Fig. 1 with measurements in the plume distinguished by the shaded bands. The 12 traverses are labeled in order of increasing downwind distance. A two-dimensional picture of the plume superimposed over the flight track is shown in Fig. 2. The path of the plume is consistent with measurements from the Fayette County ground station showing steady southerly winds changing to SSE ~2 h prior to plume sampling. An age is assigned to each traverse based on the downwind distance from the stack and the average wind velocity. Calculated plume ages range from 0.2 to 4.6 h. Subtracting these ages from the time each leg was flown yields the time of emission, ranging from 14:20 for the first leg to 11:00 for the 12th leg. Legs 9–12 were exposed to solar noon while the other legs received correspondingly less intense

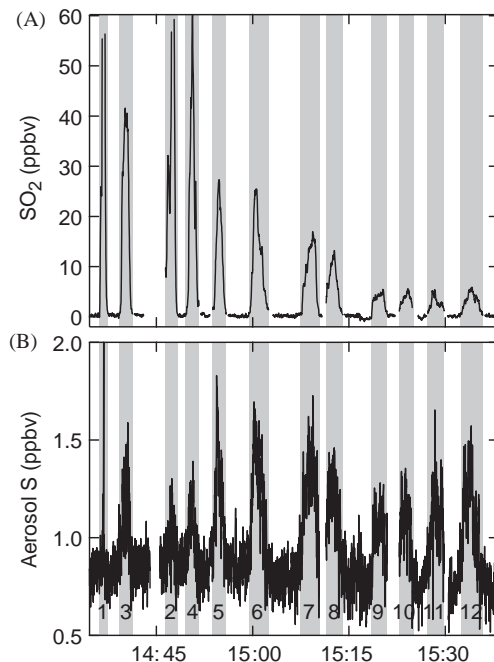


Fig. 1. Concentration of SO₂ and SO₄²⁻ vs. time with plume transects numbered in order of increasing downwind distance as shown in Fig. 2. Aerosol SO₄²⁻ calculated from PCASP size distributions assuming a composition of dry, spherical (NH₄)₂SO₄.

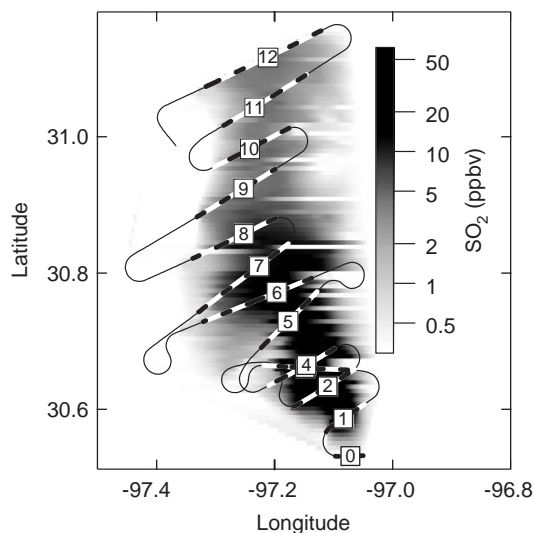


Fig. 2. Ground track of G-1 aircraft showing gridded SO₂ concentration generated from time series data shown in Fig. 1. Plume transects are numbered in order of increasing downwind distance. Dashed portions are considered in plume and correspond to shaded regions in Figs. 1, 3 and 4.

irradiation. Using these ages, various processing rates can be determined.

Fig. 1 also shows the aerosol SO_4^{2-} concentration as calculated from PCASP size distribution measurements assuming that all of the aerosol above background in the plume is $(\text{NH}_4)_2\text{SO}_4$. No adjustments due to relative humidity were made to the sizing data as the sample is dried by both the deicing heater in the optical probe and adiabatic heating from compression. Data from the PILS-IC instrument, although limited by its 3-min time resolution, yield an average NH_4^+ -to- SO_4^{2-} molar ratio of 2.5, indicating complete neutralization. A comparison of Figs. 1A and B shows that SO_4^{2-} (as calculated from aerosol volume) increases monotonically relative to SO_2 . Absolute SO_4^{2-} concentrations decrease slightly after transect 7 due to plume dispersion.

Fig. 3 shows a time sequence for NO_x and NO_y . The data in Fig. 3 have been scaled by 12% (NO_y increased) so that the ratio of NO_x to NO_y is unity at the emission source. This scaling factor is based on an observed ratio (cross-wind integrated values) of 1.03 at transect 4, corrected for oxidation of NO_x occurring between the source and transect 4 as described in a following section. The estimated $1 - \sigma$ accuracy of the NO_x and NO_y measurements is 10%, so one would expect a $1 - \sigma$ accuracy between 10 and 14% for NO_x/NO_y depending

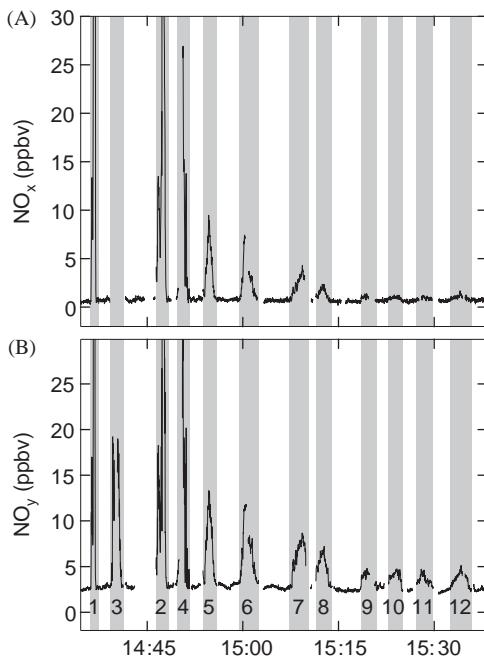


Fig. 3. Concentration of NO_x and NO_y vs. time with plumes transects numbered in order of increasing downwind distance. NO_y concentration incorporates a 12% increase as described in text.

on whether errors are common or independent. At the furthest downwind transects, the NO_x -to- NO_y ratio becomes ill-defined because plume NO_x is not much larger than background. In contrast, Fig. 1 shows that $\text{SO}_4^{2-}/\text{SO}_2$ retains a high signal-to-noise ratio far downwind.

Ozone concentrations are depicted in Figs. 4 (time series) and 5 (interpolated 2D-plot). Immediately downwind of the stack, NO emissions react with background ozone entrained in the plume causing a local reduction in O_3 . Near the source, this titration with NO reduces the O_3 concentration well below background levels to nearly zero. By transect 4, net O_3 production occurs at the plume boundaries, where the NO_x concentration is low enough to allow rapid O_3 production (Gillani et al., 1998; Ryerson et al., 1998). At a plume age of 1.5 h (transect 5), ozone production has overcome the initial loss and surplus ozone is evident across the plume. The magnitude

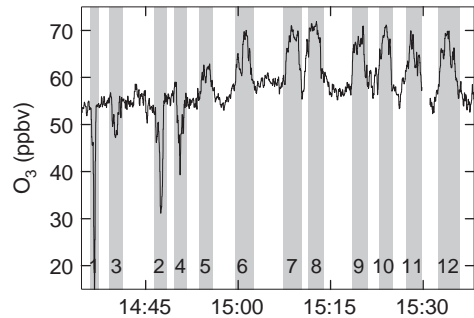


Fig. 4. Concentration of O_3 vs. time with plume transects numbered in order of increasing downwind distance.

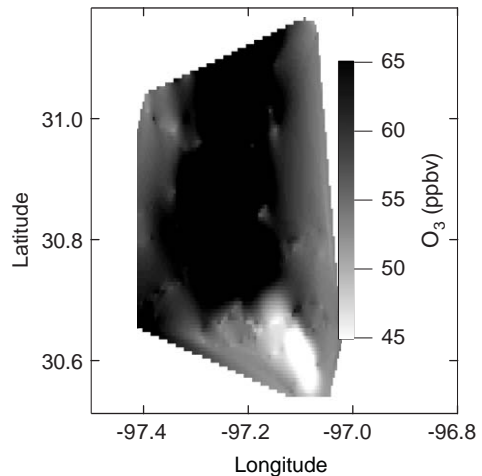


Fig. 5. Ground track of G-1 aircraft showing gridded O_3 concentration generated from time series data shown in Fig. 4.

of ozone production is not fully apparent in Figs. 4 and 5 as dilution with background air increasingly masks the appearance of new ozone with plume age.

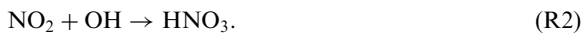
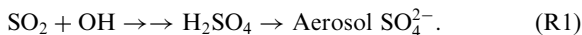
Table 1 shows that there is reasonable agreement between the S-to-N ratio obtained from the 1999 EPA emission inventory and that observed on 9 downwind traverses of the plume. We have not attempted to compare absolute values of emission fluxes because of the difficulty in determining this quantity from traverses at a single altitude. Qualitatively, it can be seen from Figs. 1 and 3 that the crosswind integrated concentrations (areas under the plume peaks) decrease significantly after traverses 8–9. It appears that vertical and/or horizontal diffusion has moved much of the plume outside of our sampling range. Sampling at multiple altitudes would be required to locate the remainder of the original emission. We recognize the displacement of the plume from the aircraft path and concentrate on comparing the ratios of various components to study transformation processes in the plume.

5. Plume chemistry

Within the power plant plume SO₂ is oxidized forming aerosol sulfate, NO₂ is oxidized to HNO₃, and O₃ is produced. From a simple model of in-plume chemistry and deposition we derive 2 values for OH concentration and an O₃ production efficiency. Changes in particle size distribution yield information on primary emissions and the aerosol formation processes.

5.1. Oxidation reactions and OH determination

As the emitted pollutants, SO₂ and NO_x, are oxidized primarily by reaction with OH, the appearance of reaction products as a function of time can be used to estimate OH concentration. The plume oxidation reactions are:



R1 is a multistep reaction with SO₂ + OH being rate determining. We will assume that NO₂ is proportional to NO_x and that HNO₃ is the dominant NO_x oxidation product as has been established in other power plant studies. Dry deposition of SO₂ and HNO₃ occur at a fast enough rate that they should be taken into account. Loss by deposition can be expressed as



The deposition velocities for SO₂ and HNO₃ are estimated to be 0.5 and 3 cm s⁻¹, respectively. Assuming

a well-mixed boundary layer with a measured depth of ~1700 m, the rates of R3 and R4 (given by deposition velocity/depth) are 1.1 and 6.4% h⁻¹. Deposition of NO_x and aerosol sulfate is slower and will be ignored. The other significant process affecting chemical concentrations is plume dispersion. In the following equations we end up using only the ratios of concentrations which are not affected by dispersion.

Reactions 1–4 lead to first-order differential equations describing the time dependence of SO₂, aerosol SO₄²⁻, NO_x, and HNO₃:

$$d\text{SO}_2/dt = -k_1\text{OH SO}_2 - k_3\text{SO}_2 \quad (1)$$

$$d\text{SO}_4^{2-}/dt = k_1\text{OH SO}_2 \quad (2)$$

$$d\text{NO}_x/dt = -k_2f\text{OH NO}_x \quad (3)$$

$$d\text{HNO}_3/dt = k_2f\text{OH NO}_x - k_4\text{HNO}_3, \quad (4)$$

where $f = \text{NO}_2/\text{NO}_x$. The value of f varies from transect to transect, in response to changing O₃, NO_x, and sunlight and exhibits a general increase as the NO_x concentration decreases. We estimate that $f = 0.85$ based on observations from the middle transects. Eqs. (1)–(4) have the solution

$$\text{SO}_2(t) = \text{SO}_2(0) \exp(-k_s t),$$

$$k_s = (k_1\text{OH} + k_3), \quad (5)$$

$$\text{SO}_4^{2-}(t) = \text{SO}_2(0)\alpha(1 - \exp(-k_s t)),$$

$$\alpha = k_1\text{OH}/(k_1\text{OH} + k_3), \quad (6)$$

$$\text{NO}_x(t) = \text{NO}_x(0) \exp(-k_2f\text{OH}t), \quad (7)$$

$$\text{HNO}_3(t) = \text{NO}_x(0)\beta[\exp(-k_4t) - \exp(-k_2f\text{OH}t)],$$

$$\beta = k_2f\text{OH}/(k_2f\text{OH} - k_4). \quad (8)$$

Eqs. (5)–(8) were used to construct the quantities, $\ln(1 - \text{SO}_4^{2-}/(\text{SO}_2 + \text{SO}_4^{2-}))$ and $\ln(\text{NO}_x/\text{NO}_y)$ which depend only on time, rate constants, f , and OH concentration. The corresponding observed quantities are determined from cross-plume integrated concentrations above background of SO₂, SO₄²⁻, NO_x, and NO_y (see Figs. 1 and 3). The SO₄²⁻ above background is determined from the PCASP using size bins smaller than $D_p = 0.4 \mu\text{m}$. Plume concentrations of larger particles could not be reliably distinguished from background values outside of the plume. A non-linear least squares program yields the OH concentration that minimizes the deviation of these OH dependent functions from the corresponding observed quantities. By neglecting the dependence of OH on downwind distance, Eqs. (1)–(8) yield an average OH that pertains to chemical conversion over the time period that the plume was sampled. Departures from that average are discussed below.

Kinetic plots are shown in Fig. 6. For sulfur chemistry, 11 of 12 traverses were used. Traverse 3 was not used because the plume was crossed at an acute angle causing a spread in downwind distance. For N chemistry an additional 2 traverses, 1 and 2, were not used because of rapidly changing and out-of-range concentrations. The fraction of SO₂ oxidized at transect 4 is 0.008. NO_x oxidation is 11.6 times faster than SO₂ ($k_2/k_1 = 9.94 \times 10^{-12}/8.57 \times 10^{-13}$; Sander et al., 2003) implying that the fraction of NO_x oxidized is 0.09. Our 12% adjustment factor for NO_x/NO_y is based on a 9% extrapolation of the observed NO_x/NO_y (1.03) at transect 4 back to zero time. This adjustment is within measurement uncertainty and is necessary to give a 100% NO_x plume at $t = 0$. Note that in both the S and N plots, oxidation starts out slow as would be expected for a high NO_x environment with suppressed photochemistry. The OH concentrations determined with and without dry deposition are given in Table 2. With deposition taken into account, OH concentrations are 8.0 and $11 \times 10^6 \text{ cm}^{-3}$ from SO₂ and NO_x kinetics, respectively. Uncertainties for OH levels based on linear regression statistics are $\pm 5 \times 10^5 \text{ cm}^{-3}$ from SO₂

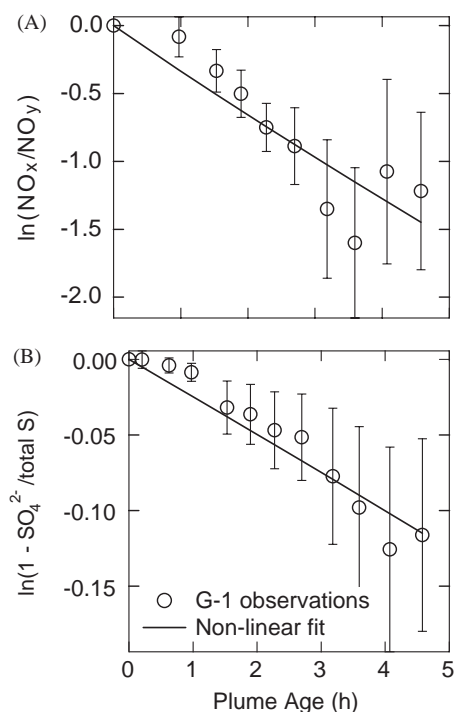


Fig. 6. Kinetic plots used to determine OH concentration from (A) oxidation of NO_x and (B) oxidation of SO₂. Error bars give $\pm 1\sigma$ uncertainties as described in text. Non-linear least-squares fit is based on Eqs. (5)–(8) describing oxidation process and deposition of SO₂ and HNO₃. OH concentrations so derived are given in Table 2.

oxidation and $\pm 8 \times 10^5 \text{ cm}^{-3}$ from NO_x oxidation. These uncertainties do not include possible systematic biases which are included in the error bars shown in Fig. 6. These error bars were calculated using instrument uncertainties (10, 10, 10, and 50%, for NO_x, NO_y, SO₂, and SO₄²⁻, respectively) plus an estimate for imprecisely known background concentrations which have to be subtracted from the plume measurements (0.15, 0.2, 0.3, and 0.1 ppbv for NO_x, NO_y, SO₂, and SO₄²⁻, respectively). Background uncertainty was determined as the low frequency variability of the out-of-plume portion of each transect. Uncertainties are combined in quadrature under the assumption that they are independent. Errors in estimating SO₂ oxidation are dominated by the uncertainty in PCASP bin size which contributes most of the 50% uncertainty of the volume measurements. Close to the power plant most of the uncertainty in NO_x conversion is due to the difficulty of measuring NO_z as the small difference between 2 large numbers. Further downwind, background subtraction becomes the largest source of uncertainty.

Fig. 7 compares SO₂ and NO_x oxidation amounts following a method used by Brock et al. (2002, 2003). A calculated curve is shown, determined from OH kinetics and deposition, using an OH concentration that is the average of that obtained for SO₂ and NO_x oxidation, i.e., OH = $9.6 \times 10^6 \text{ molecule cm}^{-3}$. Note that the calculated curve depends on OH concentration only in so far as deposition competes with oxidation. There is qualitative agreement between the calculated curve and the data points, consistent with the $1 - \sigma$ error estimates. Almost all of the discrepancy is caused by observations on transects 7–10. However, there are no obvious distinctive attributes of those transects.

5.2. Ozone production efficiency

A useful metric for the O₃-forming potential of NO_x emissions is the OPE (Trainer et al., 1993), defined here as the number of molecules of oxidant (O₃ + NO₂) formed per molecule of NO_x oxidized. We calculate this quantity for each transect as the slope of a graph of O_x vs. NO_z. Two such regression plots are illustrated in

Table 2
OH concentration from SO₂ and NO_x oxidation kinetics

Method	OH concentration (cm ⁻³)		OH ratio: NO _x /SO ₂
	SO ₂ oxidation	NO _x oxidation	
With deposition	7.96×10^6	1.13×10^7	1.42
Without deposition	8.09×10^6	1.05×10^7	1.30

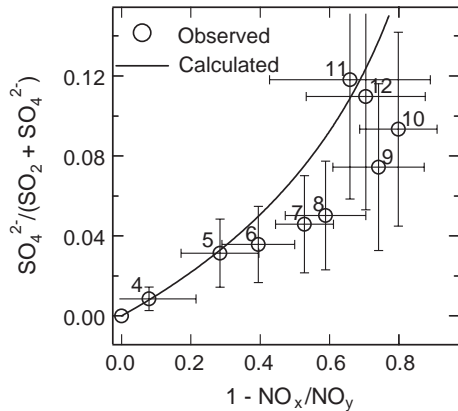


Fig. 7. Fraction of SO_2 oxidized to SO_4^{2-} vs. fraction of NO_x oxidized to NO_z for 9 traverses of the Sandow plume. Error bars give $1 - \sigma$ uncertainties as described in text. Curved line is the calculated relation between SO_2 and NO_x oxidation for an OH concentration of $9.6 \times 10^6 \text{ molecules cm}^{-3}$, an NO_2 to NO_x ratio of 0.85, and deposition velocities of SO_2 and HNO_3 of 0.5 and 3 cm s^{-1} , respectively.

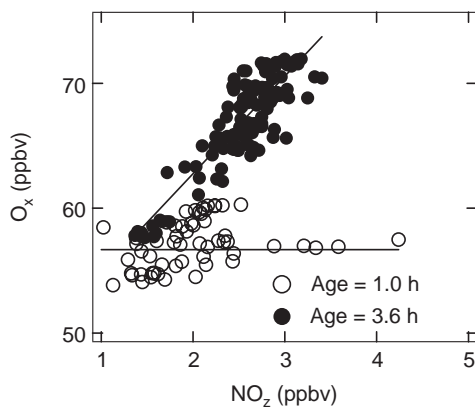


Fig. 8. Typical O_x ($\text{O}_3 + \text{NO}_2$) vs. NO_z ($\text{NO}_y - \text{NO}_x$) scatter plots shown here for traverses 4 and 10. Data points are from 1-s measurements. Lines are linear least-squares fit for each traverse. Slope gives an ozone production efficiency.

Fig. 8. Fig. 9 shows the change in OPE as a function of processing time. OPE is seen to be low in the high NO_x environment near the stack, increasing to 5–6 on the furthest downwind transects.

5.3. Aerosol concentration and size spectra

Particle size distributions are used here to characterize changes to the aerosol population due to primary emissions and gas-to-particle conversion. Figs. 10 and 11 depict aerosol number and volume size distributions over the size range covered by the PCASP (0.1–3 μm) and

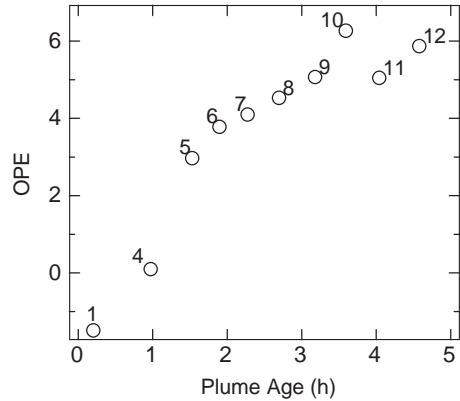


Fig. 9. Ozone production efficiency (OPE) determined as the slope of a plot of O_x ($\text{O}_3 + \text{NO}_2$) vs. NO_z ($\text{NO}_y - \text{NO}_x$) for 10 traverses of the Sandow plume. Results presented as a function of plume age with data points labeled by traverse number.

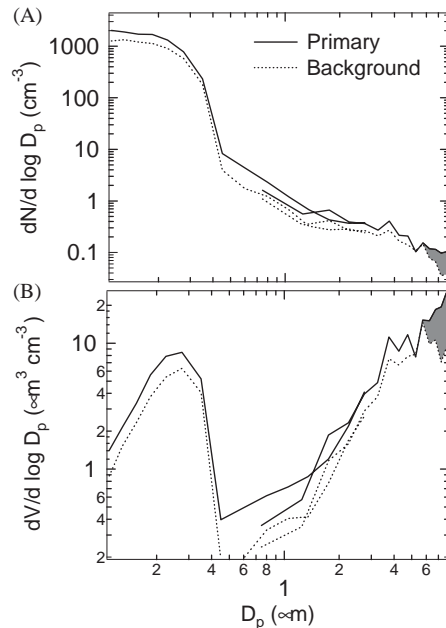


Fig. 10. Aerosol size distribution in the near-stack environment and in background air. Regions defined in Table 3. Panel (A) shows number size distribution $dN/d \log D_p$ vs. $\log D_p$. Panel (B) shows volume size distribution $dV/d \log D_p$ vs. $\log D_p$. PCASP covers the size range 0.1–3 μm ; FSSP from 0.5 to 8 μm . Filled area indicates an increase in coarse particles in near-stack environment, relative to background.

FSSP (0.5–8 μm) for data subsets representing the near stack environment and the mature plume, respectively. In each graph we include a spectrum of unperturbed background air. In all three environments, particle spectra show prominent accumulation and coarse particle modes, with a deep minimum in between. Because

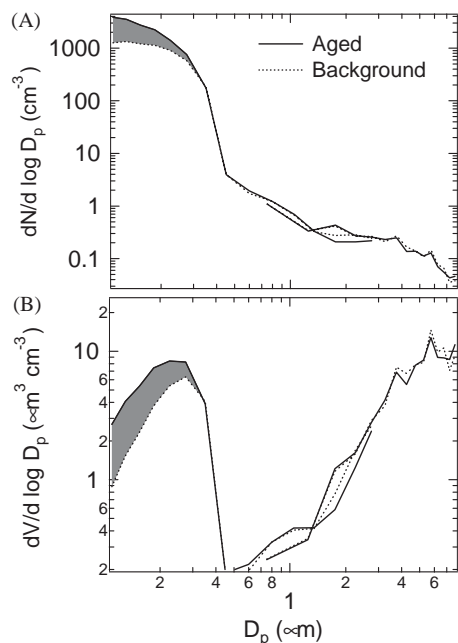


Fig. 11. Aerosol size distribution in the mature plume and in background air. Regions defined in Table 3. Format same as Fig. 10. Filled area indicates an increase in accumulation mode particles in mature plume, relative to background.

concentrations of large particles are low, results have been averaged over several minutes. In the overlap region, D_p between 0.5 and 3 μm , there is good agreement between FSSP and PCASP particle number concentration and volume. However, larger disagreements are not uncommon because of the multivalued relation between particle size and scattering in the FSSP (Leitch and Isaac, 1991). Number and volume concentrations are summarized in Table 3.

Most of the particles, by number concentration, are in the Aitken mode with D_p smaller than 0.1 μm , below the detection threshold of the PCASP. Background concentrations of CNC ($D_p > 10 \text{ nm}$) were 2000 cm^{-3} . Emissions from the Sandow stacks add large numbers of small particles. Peak concentrations observed on the close-in transects were approximately 10^5 cm^{-3} . Fig. 12 shows the number concentration of particles with $D_p > 10 \text{ nm}$ and $D_p > 0.1 \mu\text{m}$, normalized to the concurrently measured concentration of SO_2 which we use as tracer to account for plume dispersion. To a first approximation, the total number of particles ($D_p > 10 \text{ nm}$) per ppbv SO_2 is constant after transect 1. Assuming that SO_2 is a conservative tracer, this implies that the total number of particles in the plume is fixed. In contrast, the number of accumulation mode particles ($D_p > 0.1 \mu\text{m}$) per ppbv SO_2 increases two orders of magnitude as gas-to-particle conversion causes smaller particles to grow into the range detected by the PCASP

Table 3
Observed aerosol number and volume concentrations

Region ¹	PCASP	FSSP/ PCASP	FSSP
	0.1–3 μm	0.5–3 μm	0.5–8 μm
Average number concentration (cm^{-3})			
Background	528	0.84	0.55
Near-stack	769	0.60	0.82
Mature plume	1151	0.81	0.54
Average volume concentration ($\mu\text{m}^3 \text{ cm}^{-3}$)			
Background	2.81	1.06	4.10
Near-stack	4.05	0.98	6.24
Mature plume	3.98	1.22	3.98

Near-stack ($\text{SO}_2 > 30 \text{ ppbv}$), 168 s data.

Mature plume (traverses 8–12; $N_{\text{PCASP}} > 1000 \text{ cm}^{-3}$), 346 s data.

¹Background ($\text{SO}_2 < 0.75 \text{ ppbv}$; $N_{\text{PCASP}} < 600 \text{ cm}^{-3}$), 1306 s data.

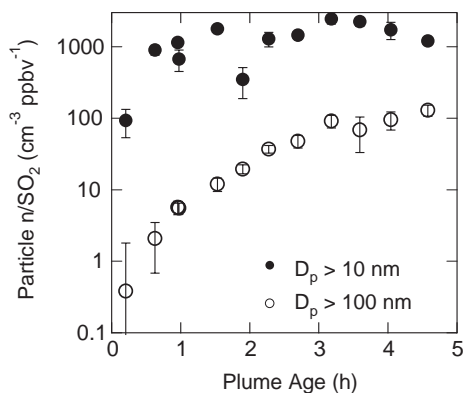


Fig. 12. Number concentration of particles with $D_p > 10 \text{ nm}$ and $D_p > 0.1 \mu\text{m}$, normalized to concurrently measured SO_2 , as a function of plume age. Ratio of particle to SO_2 concentration determined from a linear least-squares regression. Error bars are uncertainty estimate of regression slope.

(see below). The absolute number concentration of accumulation mode particles increases 2-fold in the 4.6-h plume lifetime despite the effects of dilution.

The near-stack size spectra show an increase in number and volume concentration relative to background, with the largest changes occurring in the accumulation mode and at the large size end of the coarse particle mode. The accumulation mode increase is partly due to secondary aerosol, i.e. condensation of H_2SO_4 , as it is observed to increase with time within the near-stack environment. In contrast, the near-stack coarse particle increase is only due to primary emissions as there is no mechanism to create this size particle in the atmosphere. We have tested the statistical significance of the excess FSSP volume observed in the near-stack

region with a Monte Carlo calculation, finding that no more than a few percent can be attributed to chance.

The relation between SO_2 and FSSP volume for all transects is shown in Fig. 13 where data have been binned into 4 categories according to SO_2 concentration. The intercept of a linear least-squares fit to the averaged data indicates a background FSSP volume of $4.7 \mu\text{m}^3 \text{m}^{-3}$ in reasonable agreement with background coarse particle volume presented in Table 3. Coarse particle volume associated with plume SO_2 given by the slope of the regression line is $0.06 \mu\text{m}^3 \text{m}^{-3}$ per ppbv SO_2 . Assuming a density range of $1\text{--}2 \text{ g cm}^{-3}$ for fly ash, the weight ratio of primary coarse particles to SO_2 is $0.02\text{--}0.04$, 2–4 times greater than the 0.011 ratio determined from the 1999 EPA inventory as $(\text{PM}_{10}\text{--PM}_{2.5})/\text{SO}_2$. Most of the primary coarse particle volume is in the 6–8- μm size bins (Fig. 10B). Presumably there is additional volume above the 8- μm cutoff of the FSSP, which would cause the discrepancy with the emission inventory to be greater than a factor of 2–4. It is difficult to assign an uncertainty to these figures because the response of the FSSP to nonspherical fly ash particles has not been quantified.

In the mature plume (Fig. 11), excess aerosol relative to background appears only in the size range 0.1–0.3 μm , with a 3-fold increase of particles in the smallest size bin, 0.1–0.12 μm . In the 0.1–0.3- μm size range, a growth law analysis such as described by McMurray et al. (1981), and used by Brock et al. (2002) in a recent study of power plant plumes shows that the size dependence of excess aerosol is consistent with a condensational growth mechanism. The dominant feature of the PCASP spectrum in the mature plume is therefore particles

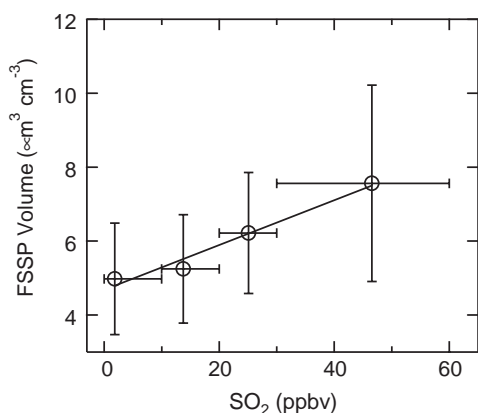


Fig. 13. Coarse particle volume determined from the FSSP vs. SO_2 concentration. Data from the Sandow plume has been averaged over 10 s intervals and binned by SO_2 concentration. Standard deviation of FSSP volume and range of SO_2 concentration within a bin are indicated by error bars. Straight line is a linear least-squares fit to the averaged data points.

growing into the observable range by vapor deposition of H_2SO_4 . However, neither a condensational mechanism nor a volume growth mechanism can explain the observation that particles with $D_p > 0.3 \mu\text{m}$ remain at background levels. Although this by itself does not totally explain the discrepancy, we note that the PCASP instrument can missize particles in the 0.35–0.65- μm range due to Mie scattering resonances, and that size bins in this range are sometimes lumped together (Leitch et al., 1991).

6. Discussion

As a qualitative test of OH concentrations and O_3 production efficiencies inferred from plume observations, we have done photochemical model simulations of conditions in the Sandow plume. A model of plume transport and chemical transformation requires more detailed meteorological information to determine dispersion than is available, so instead we have conducted a series of constrained steady-state (CSS) box model calculations meant to describe the chemistry at various points in the plume's time evolution. Given a set of concentrations for stable long-lived species this model solves the photochemical kinetic rate equation yielding the concentration of OH as well as the production and loss rates for O_3 and NO_2 (Kleinman et al., 2002). Concentrations of stable species which are not primary pollutants are specified as the average of observations made at 2 locations, one outside of the plume on transect 5 and one in a dilute region on transect 10, where hydrocarbon samples were collected. Model parameters are summarized in Table 4. Air outside of the plume is seen to have low VOC reactivity. Photolysis rates were calculated on the basis of 72% of the solar intensity at 14:00—a representative mid-point for the air parcels that we sampled in, which were emitted earlier in the day.

In order to simulate conditions in the plume, NO_x was varied from near zero to 50 ppbv and SO_2 was varied in proportion to NO_y . Plume SO_2 has a minor effect on OH, causing a 5% reduction in peak values. The effect on $\text{P}(\text{O}_3)$ and OPE is larger: a 5–10% increase under low NO_x conditions and an even larger increase in the high NO_x , VOC limited region near the stack. Changes to $\text{P}(\text{O}_3)$ are a result of SO_2 acting like a VOC in that the reaction with OH produces an HO_2 peroxy radical (Stockwell, 1994). Calculations indicate that the effects of CO (observed) and hydrocarbon emissions from Sandow (determined from the EPA emission inventory) were not significant. Fig. 14 shows calculated OH as a function of NO_x concentration. A low OH concentration and therefore a slow NO_x oxidation rate in the high NO_x environment near the source ([Karamchandani and Seigneur, 1999]) is in agreement with the kinetic data

Table 4
Inputs to photochemical box model calculation

Parameter	Value
Time	14:00 LST
O ₃	61 ppbv
CO	125 ppbv
NO _x	variable: 0.1–50 ppbv
SO ₂	variable: 0.01–135 ppbv
Anthropogenic hydrocarbon OH reactivity	0.17 s ⁻¹
Biogenic hydrocarbon OH reactivity	0.09 s ⁻¹
CH ₄	1830 ppbv
HCHO	2.6 ppbv
H ₂ O ₂	3.4 ppbv
ROOH	5.1 ppbv
solar intensity	72% of clear sky

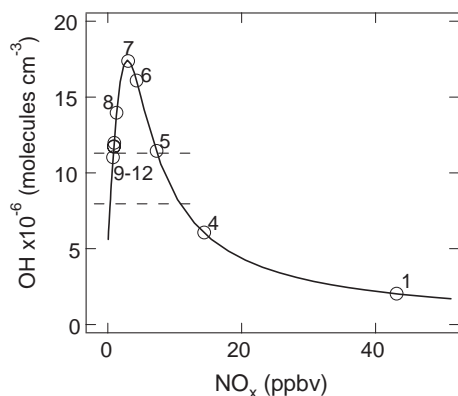


Fig. 14. OH concentration calculated from CSS box model as a function of NO_x concentration (smooth curve). Model inputs are from Table 4 except for NO_x and SO₂ which were varied to simulate the range of plume concentrations. Data points are placed on calculated curve according to the average NO_x concentration observed on the individual traverses. Dashed lines indicate OH concentrations determined from SO₂ and NO_x oxidation kinetics (see Table 2).

presented in Fig. 6. Dashed lines in Fig. 14 show the range of OH concentration deduced from SO₂ and NO_x oxidation. These OH concentrations are seen to be near the average OH experienced by an air parcel as it evolves from the high NO_x concentration of transect 1 to the sub-ppbv NO_x concentrations in transects 9–12. We take this as qualitative evidence ($\sim \pm 50\%$) of the soundness of the kinetic analysis.

The net production rate of O₃, P_N(O₃), and OPE were also determined as a function of NO_x from the CSS calculations, as shown in Fig. 15. For NO_x concentrations greater than 10 ppbv, O₃ production is slow,

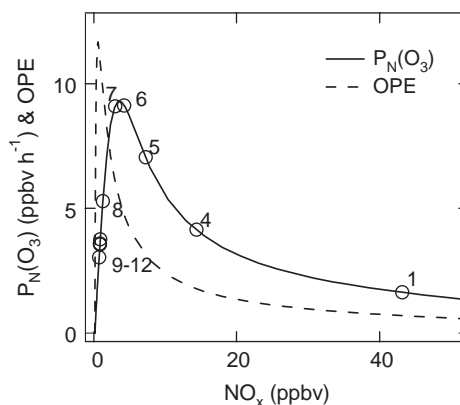


Fig. 15. Net ozone production rate, P_N(O₃), and ozone production efficiency, OPE, as a function of NO_x concentration from the same set of box model calculations used in Fig. 14. P_N(O₃) is the difference between O₃ chemical production and loss. OPE = P(O₃)/P(NO₂), where P(O₃) is the rate of O₃ production and P(NO₂) is the rate of NO₂ production, i.e., the rate of NO_x oxidation. As in Fig. 14, data points on calculated curve indicate the average NO_x concentration observed on a traverse.

<6 ppbv h⁻¹, and inefficient, OPE <2. This is due to a low VOC to NO_x ratio caused by the absence of significant quantities of biogenic or anthropogenic hydrocarbons. At lower NO_x concentration both P_N(O₃) and OPE increase. Ozone production rates and efficiencies presented in Fig. 15 are instantaneous values based on local conditions. OPE determined from measurements (Figs. 8–9), in contrast, depends on O₃ production and NO_x oxidation over the time span from emissions to measurement. Furthermore, the measured OPE is not a simple time integral of the instantaneous OPE over the time history of the emitted air parcel, so the comparison between Figs. 9 and 15 is only qualitative. Still there are a few features worth noting. The negative OPE on the first transect of Fig. 9, in part reflects the difficulty of calculating NO₂ as the difference between NO_x and NO_y when the fraction of conversion is very low. However, OPEs as negative as -1 are physically allowed. Suppose the instantaneous OPE has a constant value of *n*, i.e. reaction produces *n* molecules of O₃ for each molecule of NO_x oxidized. Then for each molecule of NO_x oxidized, the concentration of O_x is reduced by loss of one NO₂ and increased by the production of *n* molecules of O₃ resulting in a net increase of *n* - 1 molecules of O_x (Kleinman et al., 2002). An instantaneous OPE close to 1 in the high NO_x area near transect 1 implies that the measured (i.e., time averaged) OPE should be near zero, as is observed. Beyond transect 4, the instantaneous OPE increases rapidly reaching a maximum value of almost 12 near transect 12. This is also a region of high O₃ production

rates and the measured OPE of 5–6 in this region reflects the O₃ that was formed under low NO_x conditions.

7. Conclusions

Aerosol and trace gas measurements were made on 10 September 2000, during 12 transects of the lignite fired Sandow power plant plume. These transects span a 4.6 h plume lifetime centered near local noon. The appearance of aerosol SO₄²⁻ and the conversion of NO_x to oxidation products as a function of atmospheric processing time yields average OH concentrations of 8.0 and 11 × 10⁶, respectively. These estimates agree with each other within uncertainty limits. Particle size spectra determined with a PCASP are consistent with the addition of SO₄²⁻ mass by condensation onto Aitken and accumulation mode size particles. Primary emissions of coarse particles (> 5 μm) were observed. Ozone production was seen on downwind traverses but high O₃ concentrations were not reached because of extensive plume dilution. Ozone production efficiencies varied from near zero close to the stack to 5–6 on downwind low-NO_x traverses. Photochemical box model calculations were performed using measured concentrations, except for NO_x and SO₂ which were varied over a wide range to simulate the plumes time evolution. Calculations show that OH concentrations and O₃ production efficiencies are qualitatively reasonable, given that dilution causes the plume to spend much of its lifetime with NO_x concentrations below ~5 ppbv.

Acknowledgements

The authors are indebted to the pilots and flight crew of the DOE G-1 for safe operations. Special acknowledgement is due chief pilot Bob Hannigan, whose navigational skills and positional awareness enabled accurate tracing of this plume. This paper has been authored with support from the Office of Biological and Environmental Research under Contract number DE-AC02-98CH10866. The US Government retains non-exclusive, royalty free license to publish or reproduce the published form of this contribution or to allow others to do so, for US Government purposes.

References

Brock, C.A., et al., 2002. Particle growth in the plumes of coal-fired power plants. *Journal of Geophysics Research* 107 (D12), 4155.
 Brock, C.A., et al., 2003. Particle growth in urban and industrial plumes in Texas. *Journal of Geophysics Research* 108 (D3), 4111.

EPA, National Emission Inventory (NEI) Database 1999 emission values accessible from www.epa.gov/air/data/, 2004.
 Gillani, N.V., Meagher, J.F., Valente, R.J., Imhoff, R.E., Tanner, R.L., Luria, M., 1998. Relative production of ozone and nitrates in urban and rural power plant plumes 1. Composite results based on data from 10 field measurement days. *Journal of Geophysics Research* 103, 22,593–22,615.
 Hewitt, C.N., 2001. The atmospheric chemistry of sulphur and nitrogen in power plant plumes. *Atmospheric Environment* 35, 1155–1170.
 Jaenicke, R., Hanusch, T., 1993. Simulation of the optical particle counter forward scattering spectrometer probe 100 (FSSP-100), consequences for size distribution measurements. *Aerosol Science and Technology* 18, 309–322.
 Karamchandani, P., Seigneur, C. Simulations of sulfate and nitrate chemistry in power plant plumes. *Journal of Air and Waste Management Association* 49, PM175–181.
 Kleinman, L.I., Daum, P.H., Lee, Y.-N., Nunnermacker, L.J., Springston, S.R., Weinstein-Lloyd, J., Rudolph, J., 2002. Ozone production efficiency in an urban area. *Journal of Geophysics Research* 107 (D23), 4733.
 Leaitch, W.R., Isaac, G.A., 1991. Tropospheric aerosol size distributions from 1982 to 1988 over Eastern North America. *Atmospheric Environment* 25a, 601–619.
 Lee, Y.-N., Weber, R., Ma, Y., Orsini, D., Maxwell, K., Blake, D., Meinardi, S., Sachse, G., Harward, C., Chen, T.-Y., Thornton, D.C., Tu, F.H., Bandy, A.R., 2003. Airborne measurement of inorganic ionic components of fine aerosol particles using the PILS-IC technique during ACE-ASIA and TRACE-P. *Journal of Geophysics Research* 108, 8646.
 Liu, Y., Daum, P.H., 2000. The effect of refractive index on size distributions and light scattering coefficients derived from optical particle counters. *Journal of Aerosol Science* 8, 945–957.
 Luria, M., Tanner, R.L., Imhoff, R.E., Valente, R.J., Bailey, E.M., Mueller, S.F., 2000. Influence of natural hydrocarbons on ozone formation in an isolated power plant plume. *Journal of Geophysics Research* 105, 9177–9188.
 Malm, W.C., Schichtel, B.A., Pitchford, M.L., Ashbaugh, L.L., Eldred, R.A., 2004. Spatial and monthly trends in speciated fine particle concentration in the United States. *Journal of Geophysics Research* 109, D03306.
 McMurry, P.H., Rader, D.J., Stith, J.L., 1981. Studies of aerosol formation in power plant plumes—I Growth laws for secondary aerosols in power plant plumes: implications for chemical conversion mechanisms. *Atmospheric Environment* 15, 2315–2327.
 Moore II, K.G., et al., 2004. A comparison of similar aerosol measurements made on the NASA P3-B, DC-8, and NSF C-130 aircraft during TRACE-P and ACE-Asia. *Journal of Geophysics Research* 109, D15S15.
 Nunnermacker, L.J., Imre, D., Daum, P.H., Kleinman, L., Lee, Y.-N., Lee, J.H., Springston, S.R., Newman, L., Weinstein-Lloyd, J., Luke, W.T., Banta, R., Alvarez, R., Senff, C., Sillman, S., Holdren, M., Keigley, G.W., Zhou, X., 1998. Characterization of the Nashville urban plume on July 3 and July 18, 1995. *Journal of Geophysics Research* 103, 28,129–28,148.
 Nunnermacker, L.J., Kleinman, L.I., Imre, D., Daum, P.H., Lee, Y.-N., Lee, J.H., Springston, S.R., Newman, L.,

- Gillani, N., 2000. NO_y lifetimes and O_3 production efficiencies in urban and power plant plumes: analysis of field data. *Journal of Geophysics Research* 105, 9165–9176.
- Ryerson, T.B., Buhr, M.P., Frost, G.J., Goldan, P.D., Holloway, J.S., Hübler, G., Jobson, B.T., Kuster, W.C., McKeen, S.A., Parrish, D.D., Roberts, J.M., Sueper, D.T., Trainer, M., Williams, J., Fehsenfeld, F.C., 1998. Emissions lifetimes and ozone formation in power plant plumes. *Journal of Geophysics Research* 103, 22,569–22,583.
- Ryerson, T.B., Trainer, M., Holloway, J.S., Parrish, D.D., Huey, L.G., Sueper, D.T., Frost, G.J., Donnelly, S.G., Schauffler, S., Atlas, E.L., Kuster, W.C., Goldan, P.D., Hübler, G., Meagher, J.F., Fehsenfeld, F.C., 2001. Observations of ozone formation in power plant plumes and implications for ozone control strategies. *Science* 292, 719–723.
- Sander, S.P., Golden, D.M., Kurylo, M.J., Huie, R.E., Orkin, V.L., Moortgat, G.K., Ravishankara, A.R., Kolb, C.E., Molina, M.J., Finalyson-Pitts, B.J., 2003. *Chemical Kinetics and Photochemical Data for Use in Atmospheric Studies*, Evaluation Number 14, JPL Publication 02-25. Jet Propulsion Laboratory, Pasadena.
- Stockwell, W.R., 1994. The effect of gas-phase chemistry on aqueous-phase sulfur dioxide oxidation rates. *Journal of Atmospheric Chemistry* 19, 317–329.
- Trainer, M., et al., 1993. Correlation of ozone with NO_y in photochemically aged air. *Journal of Geophysics Research* 98, 2917–2925.